Electrocardiographic Simulation on Coupled Meshfree-BEM Platform

Linwei Wang[1], Ken C.L. Wong[1], Heye Zhang[2], and Pengcheng Shi[1]

[1] Computational Biomedicine Laboratory
Rochester Institute of Technology, Rochester, NY, USA
maomaowlw@mail.rit.edu
[2] Bioengineering Institute, University of Auckland, Auckland, New Zealand

Abstract. The foremost premise for the success of noninvasive volumetric myocardial transmembrane (TMP) imaging from body surface potential (BSP) recordings is a realistic yet efficient electrocardiographic model which relates volumetric myocardial TMP distribution to BSP distribution. With a view towards this inverse problem, the heart-torso representation and the associated TMP-to-BSP model should balance the accuracy of the model with the feasibility of TMP reconstruction. We present a novel coupled meshfree-BEM platform to this TMP-to-BSP modeling and perform electrocardiographic simulations of various cardiac conditions on personalized heart-torso structures. Simulated QRS integral maps, BSPMs and ECG leads are consistent with existent experimental studies, verifying the plausibility of the presented platform.

1 Introduction

Noninvasive imaging of volumetric myocardial transmembrane potential (TMP) dynamics aims at quantitative reconstructions of TMP dynamics inside the heart from body surface potential (BSP) sequence. The foremost premise for its success is a forward electrocardiographic model which links volumetric myocardial TMP distribution with BSP distribution. With a view towards the inverse problem of TMP reconstruction, this TMP-to-BSP model and the associated representation of the underlying heart-torso structures should emphasize the balance between the accuracy of the models with the feasibility of TMP reconstruction.

The common description of TMP-to-BSP mapping is based on the biodomain theory, where any point in the myocardium is considered to be in either the intra- or extra-cellular space [1]. Usually it is reduced to a boundary element (BE) formulation by ignoring the conductive anisotropy and inhomogeneity in both spaces [2]. As a result, it considers only TMP activity on heart surfaces. By considering the electrical anisotropy in both spaces, the finite element (FE) formulation is able to investigate volumetric electrical conduction within the myocardial mass [3]. Meanwhile it increases the problem size by considering extracellular potential in the myocardium.

This paper presents a coupled meshfree-BEM platform for TMP-to-BSP modeling to combine the advantage of BEM- and FEM-based approaches. To investigate the volumetric myocardial TMP dynamics, meshfree points are used to

N. Ayache, H. Delingette, and M. Sermesant (Eds.): FIMH 2009, LNCS 5528, pp. 162–171, 2009.

detail the anatomical structure, as well as the anisotropy and heterogeneity, of the 3D myocardium. Meanwhile, to emphasize the accuracy of geometrical modeling and relax unnecessary restrictions on conductivie anisotropy or inhomogeneity of different torso tissues, we assume the torso as an isotropic and homogeneous volume conductor, represented with boundary elements on the body surface. By emphasizing the anisotropy for active current conduction but neglecting that for passive currents, this approach allows the investigation of volumetric TMP inside the myocardium while discarding irrelevant variables to reduce model complexity.

The accuracy and convergency of this approach has been verified by analytical solutions on a synthetic geometry of two concentric spheres [4]. In this paper, electrocardiographic simulations of normal cardiac conditions, ventricular pacing, bundle branch blocks (BBB) and myocardial infarction are carried out on personalized heart-torso structures. Simulated BSP map sequences, QRS integral (QRSI) maps and 12 ECG leads are compared to existent experimental studies, demonstrating the plausibility of the presented coupled meshfree-BEM platform in TMP reconstruction.

2 Methods

2.1 Personalized Heart-Torso Structures

After segmenting the short-axis cardiac MRI slice by slice and building a smoothed mesh for the heart surfaces, the 3D heart wall is represented by a cloud of points (meshfree points) inside the surface mesh. Myocardial conductive anisotropy is considered by mapping volumetric fiber structures from the fibrous structure of the canine heart in [5]. Heterogeneity of TMP shapes in the epi-, endo- and mid-myocardial regions [6] is also taken into account. For a flexible control on the simulation of various cardiac conditions, the LV wall is divided into 17 segments by AHA consensus [7]. Because the torso geometry is the primary factor affecting TMP-to-BSP relationship [8], the volume conductor of torso is assumed as isotropic and homogeneous. It is described by triangulated body surface, obtained by deforming a reference torso model to match patient's image data [9].

2.2 Volumetric TMP Dynamics

Myocardial TMP dynamics is described by the 2-variable diffusion-reaction system from [10]:

$$\begin{cases} \frac{\partial u}{\partial t} = \nabla \cdot (\mathbf{D}\nabla u) + ku(u-a)(1-u) - uv \\ \frac{\partial v}{\partial t} = -e(v + ku(u-a-1)) \end{cases} \tag{1}$$

where u stands for TMP and v for recovery current. $\mathbf{D}$ is the diffusion tensor and $\nabla \cdot (\mathbf{D}\nabla u)$ accounts for the electrical propagation. Parameters e, k and a determine individual TMP shapes.

2.3 TMP-to-BSP Mapping

Potential distribution within the torso is described by the quasi-static approximation of Maxwell's equations [11]. Within the myocardium volume Ω_h, the bidomain theory [1] defines the distribution of extracellular potentials ϕ_e as a result of the gradients of TMP:

$$\nabla\cdot((\mathbf{D}_i(\mathbf{r})+\mathbf{D}_e(\mathbf{r}))\nabla\phi_e(\mathbf{r})) = \nabla\cdot(\mathbf{D}_k(\mathbf{r})\nabla\phi_e(\mathbf{r})) = \nabla\cdot(-\mathbf{D}_i(\mathbf{r})\nabla u(\mathbf{r})) \quad \forall\mathbf{r}\in\Omega_h \tag{2}$$

where $\mathbf{r}$ stands for the spatial coordinate. $\mathbf{D}_i$ and $\mathbf{D}_e$ are the effective intracellular and extracellular conductivity tensor, and their summations $\mathbf{D}_k$ is termed as the bulk conductivity tensor. In the region $\Omega_{t/h}$ bounded by the heart surfaces and body surface, potentials ϕ_t are calculated assuming that no other active electrical source exists within the torso:

$$\nabla\cdot(\mathbf{D}_t(\mathbf{r})\nabla\phi_t(\mathbf{r})) = 0 \qquad \forall\mathbf{r}\in\Omega_{t/h} \tag{3}$$

where $\mathbf{D}_t$ is torso conductivity tensor.

Because the anisotropic ratio of $\mathbf{D}_k$ is a magnitude smaller than that of $\mathbf{D}_i$, we only retain the anisotropy of $\mathbf{D}_i$ to reduce model complexity. Regarding the tissue inhomogeneity, we have justified the validity of the homogeneous torso model in TMP reconstruction [4]. Accordingly, (2, 3) is simplified into a single Poisson equation describing potential distribution $\phi(\mathbf{r})$ within the homogeneous volume conductor Ω_t:

$$\sigma\nabla^2\phi(\mathbf{r})) = \nabla\cdot(-\mathbf{D}_i(\mathbf{r})\nabla u(\mathbf{r})) \quad \forall\mathbf{r}\in\Omega_t \tag{4}$$

and it is assumed that no current leaves the body surface Γ_t: $\frac{\partial\phi_t(\mathbf{r})}{\partial\boldsymbol{n}} = 0, \forall\mathbf{r}\in\Gamma_t$.

By the *direct method* solution in BEM [12], (4) is reformulated into:

$$\begin{aligned} c(\xi)\phi(\xi) + \int_{\Gamma_t}\phi(\mathbf{r})q^*(\xi,\mathbf{r})\,\mathrm{d}\Gamma_t - \int_{\Gamma_t}(\frac{\partial\phi(\mathbf{r})}{\partial\boldsymbol{n}})\phi^*(\xi,\mathbf{r})\,\mathrm{d}\Gamma_t \\ = \int_{\Omega_t}\frac{(\nabla\cdot(\mathbf{D}_i\nabla u(\mathbf{r})))\phi^*(\xi,\mathbf{r})}{\sigma}\,\mathrm{d}\Omega_t \end{aligned} \tag{5}$$

where $c(\xi)$ is determined by surface smoothness of any point ξ on Γ_t. $\boldsymbol{n}$ is the outward normal vector of boundary surfaces. $\phi^*(\xi,\mathbf{r})$ and $q^*(\xi,\mathbf{r})$ are the so-called fundamental solution and its normal derivative [12].

The volume integral on the right hand side (rhs) of (5) is commonly approximated as a summarization of several current dipoles [13]. Instead, we introduce meshfree approximation based on moving least squares (MLS) [14] into (5) for a simpler yet more direct calculation of the volume integral. It is shown in [13] that in most cases, MLS methods are identical to kernel methods and may serve as a partition of unity. Further applying the BEM [12] to the boundary integral in (5) [4], we obtain the linear relationship between volumetric TMP and BSP:

$$\mathbf{\Phi} = \mathbf{HU} \tag{6}$$

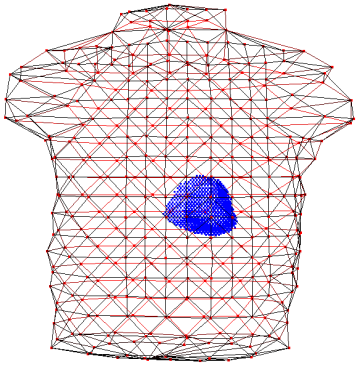

Fig. 1. Personalized heart-torso structure on coupled meshfree-BEM representation, where the ventricles are represented with a cloud of 3999 meshfree points and the torso by triangulated body surface with 370 vertices

where $\mathbf{U}$ consists of u from all meshfree points inside the myocardium and $\mathbf{\Phi}$ contains ϕ from all vertices on the body surface.

When (2) is reduced to a BE formulation [2], the conductive anisotropy and inhomogeneity in both intra- and extra-cellular spaces are ignored, and therefore only TMP activity on heart surfaces are considered. On the other side, the FE formulation considers the conductive anisotropy in both space and therefore allows the investigation of volumetric electrical conduction within the myocardial mass [3]. However, it increases the problem size by considering extracellular potentials in the 3D myocardium. This approach combines the advantages of previous BE- and FE-based efforts by emphasizing the electrical anisotropy for active current conduction but neglecting that for passive currents. It is able to study TMP activity inside the 3D myocardium and preserves the primary factors to TMP-to-BSP modeling, including 3D anisotropic heart structures and relative heart-torso positions. Meanwhile, it avoids excessive variables and focus only on TMP and BSP, the two vectors of direct interest to TMP reconstruction.

3 Results

Electrocardiographic simulations of normal cardiac conditions, ventricular pacing, BBB and MI are performed on personalized heart-torso structures. The cardiac MRIs provided by [15] contain 9 slices from apex to base, with 8mm inter-slice spacing and 1.33mm/pixel in-plane resolution. Anatomical locations of 123 electrodes on the body surface are also available. Fig 1 (b) illustrates this personalized combined heart-torso model, where the torso is represented by triangulated body surface with 736 elements and 370 vertices, and the 3D ventricular mass by 3339 meshfree points with detailed fiber structure. Simulated BSPM sequences exhibit the spatiotemporal evolution of BSP distributions. QRSI maps are generated by integrating BSPs over the QRS interval, and 12 ECG leads are calculated according to the given electrode locations. These results are compared to published experimental studies for verification.

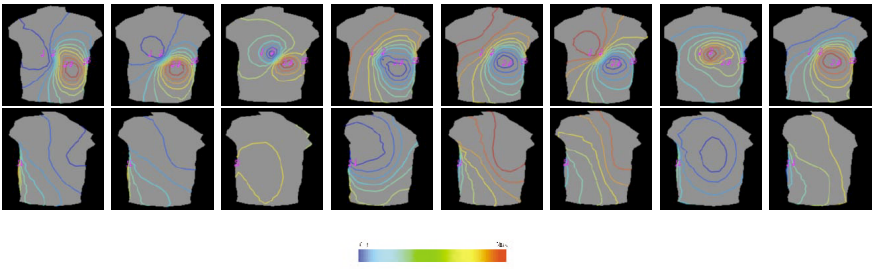

Fig. 2. Simulated BSPM isochrone sequence during normal cardiac electrical activation. The color encodes normalized BSP value.

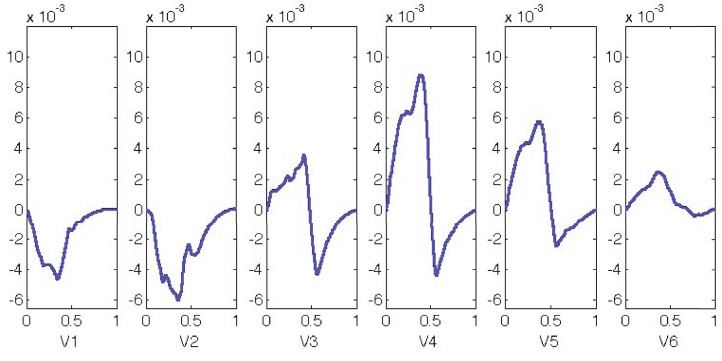

Fig. 3. Simulated normal QRS morphology of lead $V1$ - $V6$. The time course (x-axis) is normalized by the QRS interval and ECG values (y-axis) are scaled.

3.1 Normal Cardiac Conditions

Since the ventricular conduction system is not included in the current heart model, endocardial areas of earliest ventricular excitation are determined according to the experimental study of [16]. In the simulated BSPM sequence (Fig. 2), the potential maximum initially resides on the anterior thorax and the minimum on the back. The minimum then moves over the right shoulder onto the anterior region, while the positive potentials cover the back. In the end, the maximum rotate back to the superior part of the chest. Fig. 3 displays the simulated 6 precordial leads, where $V1$ shows a dominant negative defect and $V3 - V6$ display dominant positivity. Besides, since cardiac activation progresses from the thinner right ventricle across the thicker left ventricle, positive R wave increases in amplitude and duration from leads $V1$ to $V4$, while S wave is large in $V1$, larger in $V2$, and progressively smaller from $V3$ through $V6$. These results are consistent with the BSP morphology known for normal subjects [17].

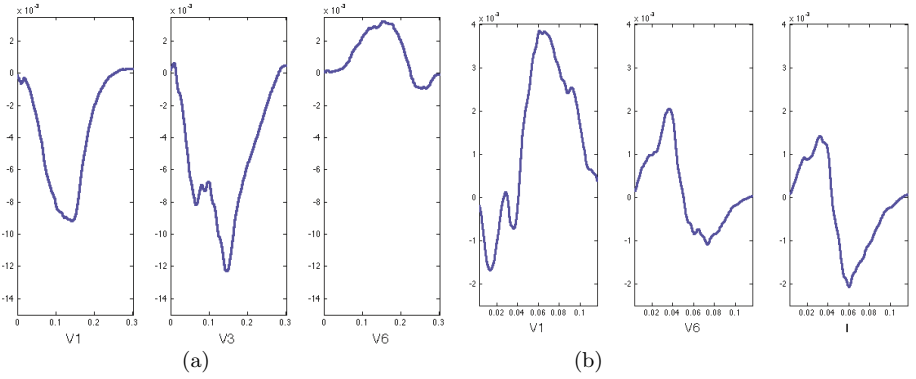

Fig. 4. Simulated QRS morphology in BBB conditions. (a) Lead $V1, V2$ and $V6$ for LBBB. (b) Lead $V1, V6$ and I for RBBB. The time course (x-axis) is normalized by the QRST interval and ECG values (y-axis) are scaled.

3.2 Bundle Branch Block (BBB)

Different BBB conditions are simulated by removing corresponding sites of earliest exitation in the ventricles. The results of ECG leads comply with standard diagnostic criteria [17]. For LBBB, since the activation proceeds sequentially from the interventricular septum to the lateral LV wall, the characteristic changes of the QRS complex are the monophasic QS morphology in $V1$, broad R wave in $V6$ and minimal R wave in $V2$ (Fig. 4 (a)). In comparison, since the RV contributes minimally to QRS complex, RBBB produces little distortion to the normal QRS morphology. As show in Fig. 4 (b), the abnormality is usually marked by the presence of a late prominent positive in $V1$, and a wide S wave in V6 and I.

3.3 Ventricular Pacing (Ectopic Activity)

The atlas of body surface QRSI map has been established for identifying ectopic ventricular activation [18]. This study simulates ventricular pacing cases in [18] for a comparison with the QRSI map atlas established therein. Fig. 5 lists examples of QRSI maps generated from ventricular pacing at 6 endocardial sites at the basal LV and the apical level. When the pacing site advances horizontally from lateral, anterior, septal to inferior part at basal LV endocardium (Fig. 5 (a)), the anticlockwise rotation of the potential maximum and minimum reported in [18] is observed. During apical pacing (Fig. 5 (b)), the minimum lies at a quite similar location on the lower anterior thorax while the maximum moves from the upper front to upper back with the pacing site moving from apical inferior to apical septal. In addition, LBBB morphology (negative QRS polarity in V1) is noted in QRSI maps for all apical pacing and LV basal septum pacing. All these observations, including the distribution, location and rotation of potential extreme, are in good accordance with the atlas [18].

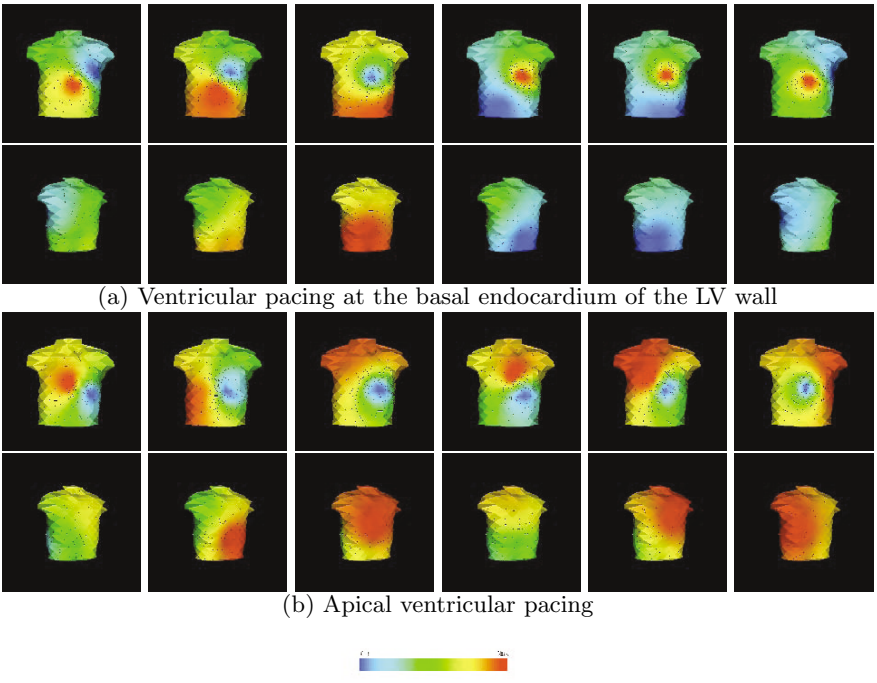

(a) Ventricular pacing at the basal endocardium of the LV wall

(b) Apical ventricular pacing

Fig. 5. Simulated QRSI maps for different ventricular pacing cases. (a) Left to right: pacing sites change horizontally from anterior-lateral, anterior, anterior-septal, inferior-septal, inferior to inferior-lateral parts of the basal LV wall. (b) Left to right: pacing sites at lateral, anterior, septal and inferior apical endocardium of the LV, LV apex and RV apex. The color encodes the integrated BSP values during QRS interval.

We have simulated BSP sequences for several typical ventricular pacing cases, and all the results are in agreement with the experimental recordings by [18]. Fig. 6 exemplifies the simulated BSP map sequence for anterior-lateral pacing at the middle LV endocardium. At the beginning, the minimum shifts from the upper right anterior thorax toward the left back while the maximum moves from the lower left anterior part to the right part of the chest. It is followed by a stable bipolar BSPM pattern featuring clockwise rotation of potential extreme. By the end of the ventricular activation, regions of positive and negative potentials appear almost vertical on the anterior and posterior torso.

3.4 Myocardial Infarction (MI)

Various locations of infarct substrates are selected from the 17 LV segments. Electrophysiological properties for infarct tissues are modified so that TMP shapes show progressively reduced action potential duration and magnitude, until no activation could be stimulated in the center of the infarcted region. Fig. 7 lists the simulated BSPMs at the beginning of the S-T segment for transmural infarction at the middle anterior, inferior and lateral walls of the LV. As reported

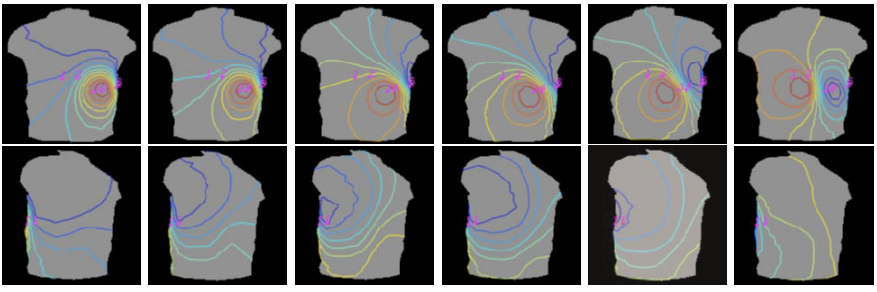

Fig. 6. Simulated BSPM isochrone sequence of the anteriorlateral pacing at the middle endocardium of LV. The color bar is the same as in Fig. 2.

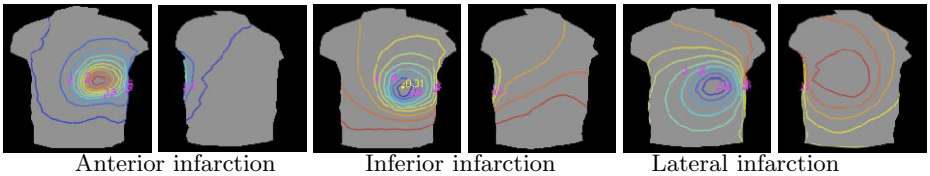

Fig. 7. Simulated BSPM isochrone map at the beginning of the S-T segment for 3 different MI conditions. The color bar is the same as in Fig. 2.

in [19], BSPMs display a potential maximum facing the infarct location and an opposite potential minimum.

4 Conclusions and Discussions

To provide an applicable heart-tosro representation and TMP-to-BSP model for noninvasive volumetric myocardial TMP imaging from BSPs, we present a novel coupled meshfree-BEM platform and verify its plausibility by electrocardiographic simulations of different cardiac conditions on realistic heart-torso structures. To improve the accuracy of simulated ECG leads, firstly, models with more complexity and detailedness are needed for a more realistic description of volumetric electrical activity of the heart. Geometrical modeling, such as the relative position between the heart and the electrodes, is another important factor on the electrocardiographic simulation. Meanwhile, a more realistic and detailed heart model would largely improve the accuracy of the simulated ECGs. For instance, the errors caused by incorrect locations of earliest ventricular excitation could be reduced by incorporating the ventricular conduction system into the heart model. By taking into account transmural electrical heterogeneity, this study avoids generating incorrect T waves as a reverse of the QRS complex. Nevertheless, more accurate divisions among the epi-, endo- and mid-myocardial

cells are desired. Besides, by including the atrium into the heart model, P wave could be generated in the simulated ECGs.

References

1. Henriquez, C.S.: Simulating the electrical behaviour of cardiac tissue using the bidomain model. Crit. Rev. Biomed. Eng. 21, 1–77 (1993)
2. Fischer, G., Tilg, B., Wach, P., Lafter, G., Rucker, W.: Analytical validation of the bem-application of the bem to the electrocardiographic forward and inverse problem. Comput. Methods Programs Biomed. 55, 99–106 (1998)
3. Fischer, G., Tilg, B., Modre, R., Huiskamp, G.J.M., Fetzer, J., Rucker, W., Wach, P.: A bidomain model based bem-fem coupling formulation for anisotropic cardiac tissue. Ann. Biomed. Eng. 28, 1229–1243 (2000)
4. Wang, L., Zhang, H., Wong, K.C., Shi, P.: Coupled meshfree-bem platform for electrocardiographic simulation: Modeling and validations. In: Dohi, T., Sakuma, I., Liao, H. (eds.) MIAR 2008. LNCS, vol. 5128, pp. 98–107. Springer, Heidelberg (2008)
5. Nash, M.: Mechanics and Material Properties of the Heart using an Anatomically Accurate Mathematical Model. PhD thesis, Univ. of Auckland, New Zealand (May 1998)
6. Yan, G.X., Shimizu, W., Antzelevitch, C.: Charactertistics and distribution of m cells in arterially perfused canine left ventricular wedge preparations. Circ. 98, 1921–1927 (1998)
7. Cerqueira, M.D., Weissman, N.J., Dilsizian, V., Jacobs, A.K., Kaul, S., Laskey, W.K., Pennell, D.J., Rumberger, J.A., Ryan, T., Verani, M.S.: Standardized myocardial segmentation and nomenclature for tomographic imaging of the heart. Circ. 105, 539–542 (2002)
8. Brandley, C.P., Pullan, A.J., Hunter, P.J.: Effects of material properties and geometry on electrocardiographic forward simulations. Ann. Biomed. Eng. 28, 721–741 (2000)
9. Cheng, L.: Non-invasive Electrical Imaging of the Heart. PhD thesis, Univ. of Auckland, New Zealand (2001)
10. Aliev, R.R., Panfilov, A.V.: A simple two-variable model of cardiac excitation. Chaos, Solitions & Fractals 7(3), 293–301 (1996)
11. Plonsey, R.: Bioelectric phenonmena. McGraw-Hill, New York (1969)
12. Brebbia, C.A., Telles, J.C.F., Wrobel, L.C.: Boundary element techniques: theory and applications in engineering. Springer, Heidelberg (1984)
13. Barnard, A.C.L., Duck, I.M., Lynn, M.L.: The application of electromagentic theroy to electrocardiology. Biophys. J. 7, 443–462 (1967)
14. Belytschko, T., Krongauz, Y., Organ, D., Fleming, M., Krysl, P.: Meshless methods: An overview and recent developments. Computer Methods in Applied Mechanics and Engineering 139(1), 3–47 (1996)
15. Goldberger, A.L., Amaral, L.A.N., Glass, L., Hausdorff, J.M., Ivanov, P.C., Mark, R.G., Mietus, J.E., Moody, G.B., Peng, C.K., Stanley, E.: Physiobank, physiotoolkit, and physionet components of a new research resource for complex physiological signals. Cric. 101, e215–e220 (2000)
16. Durrur, D., Dam, R., Freud, G., Janse, M., Meijler, F., Arzbaecher, R.: Total excitation of the isolated human heart. Comp. Methods Appl. Mech. Eng. 41(6), 899–912 (1970)

17. Wagner, G.S.: Marriott's practical electrocardiography. Lippincott williams & wilkins, Philadelphia (2001)
18. SippensGroenewegen, A., Spekhorst, H., van Hemel, N.M., Kingma, J.H., Hauer, R.N., Janse, M.J., Dunning, A.J.: Body surface mapping of ectopic left and right ventricular activation. QRS spectrum in patients without structural heart disease. Circ. 82, 879–896 (1990)
19. Miller, W.T., Geselowitz, D.B.: Simulation sutdies of the electrocardiogram. ii. ischemia and infarction. Circ. Res. 43, 315–323 (1978)